

Observation of Flat Band, Dirac Nodal Lines and Topological Surface States in Kagome Superconductor CsTi_3Bi_5

Jiangang Yang^{1,2,‡}, Yuyang Xie^{1,2,‡}, Zhen Zhao^{1,2,‡}, Xinwei Yi^{2,3,‡}, Taimin Miao^{1,2}, Hailan Luo^{1,2}, Hao Chen^{1,2}, Bo Liang^{1,2}, Wenpei Zhu^{1,2}, Yuhan Ye^{1,2}, Jing-Yang You⁴, Bo Gu^{2,3}, Shenjin Zhang⁵, Fengfeng Zhang⁵, Feng Yang⁵, Zhimin Wang⁵, Qinjun Peng⁵, Hanqing Mao^{1,2,6}, Guodong Liu^{1,2,6}, Zuyan Xu⁵, Hui Chen^{1,2,3}, Haitao Yang^{1,2,3}, Gang Su^{2,3*}, Hongjun Gao^{1,2,3,*}, Lin Zhao^{1,2,6,*} and X. J. Zhou^{1,2,6,*}

¹*Beijing National Laboratory for Condensed Matter Physics,
Institute of Physics, Chinese Academy of Sciences, Beijing 100190, China.*

²*University of Chinese Academy of Sciences, Beijing 100049, China.*

³*CAS Center for Excellence in Topological Quantum Computation,
University of Chinese Academy of Sciences, Beijing 100190, China*

⁴*Department of Physics, Faculty of Science,
National University of Singapore, Singapore 117551, Singapore.*

⁵*Technical Institute of Physics and Chemistry,
Chinese Academy of Sciences, Beijing 100190, China.*

⁶*Songshan Lake Materials Laboratory,
Dongguan, Guangdong 523808, China.*

(Dated: December 8, 2022)

Abstract

A kagome lattice of 3d transition metals hosts flat bands, Dirac fermions and saddle points. It provides a versatile platform for achieving topological superconductivity, anomalous Hall effect, unconventional density wave order and quantum spin liquid when the strong correlation, spin-orbit coupling or magnetic order are involved in such a lattice. Here, using laser-based angle-resolved photoemission spectroscopy in combination with density functional theory calculations, we investigate the electronic structure of the newly discovered kagome superconductor CsTi_3Bi_5 , which is isostructural to the AV_3Sb_5 ($\text{A}=\text{K}, \text{Rb}$ or Cs) kagome superconductors and possesses a perfect two-dimensional kagome network of Titanium. We directly observed a strikingly flat band derived from the local destructive interferences of Bloch wave functions within the kagome lattices. We also identify the type-II Dirac nodal loops around the Brillouin zone center, the type-III Dirac nodal loops around the zone corners and type-III Dirac nodal lines along the k_z direction. In addition, around the Brillouin zone center, Z2 nontrivial topological surface states are also observed which is formed from the band inversion due to strong spin orbital coupling. The simultaneous existence of such multi-sets of nontrivial band structures in one kagome superconductor not only provides good opportunities to study related physics in the kagome lattice but also makes CsTi_3Bi_5 an ideal system to realize novel quantum phenomena by manipulating its chemical potential with chemical doping or pressure.

Quantum materials with layered kagome structures have drawn enormous attentions because such a two-dimensional (2D) network of corner-sharing triangle lattice can give rise to many exotic quantum phenomena, such as spin liquid phases[1–4], topological insulator and topological superconductor[5–7], fractional quantum Hall effect[8], quantum anomalous Hall effect[9, 10] and unconventional density wave orders[11–16]. All these exotic quantum phenomena are thought to originate from the unique electronic structure of the kagome lattice including flat bands, Dirac cones and saddle points when the spin orbital coupling, magnetic ordering or strong correlation are taken into consideration. Nevertheless, the definitive identification of such unique electronic structures in the kagome materials are still scarce and the underlying mechanism to induce those exotic quantum phenomena from such electronic structures remains illusive. For example, the kagome superconductors AV_3Sb_5 ($A=K, Rb$ or Cs) [17], which have been the focus of recent extensive research, exhibit anomalous Hall effect[18], unconventional charge density wave (CDW)[15, 19–25], pairing density wave[14] and possible unconventional superconductivity and nematic phase[13, 18, 25, 26]. However, the nature and origin of these novel physical properties are still in hot debates. Even for the clear identification of the flat band, it still needs further investigations. It is significant to establish a relationship between the unique electronic structures of the kagome lattice and its novel quantum phenomena.

$CsTi_3Bi_5$ is a newly discovered kagome superconductor which is isostructural to the AV_3Sb_5 superconductors (Fig. 1a)[27]. The titanium atoms form a kagome network with the bismuth atoms lying in the hexagons and above and below the triangles (Figs. 1a and 1b). Magnetic susceptibility and electrical resistivity measurements of $CsTi_3Bi_5$ indicate that there is no phase transition observed down to the superconducting transition at 4.8 K[28]. This is different from CsV_3Sb_5 that exhibits a CDW transition around 94 K[17]. The similar crystal structure but the absence of the CDW order in $CsTi_3Bi_5$ provide a good opportunity to study the intrinsic electronic structure of the kagome lattice with reference to CsV_3Sb_5 and understand the origin of various quantum phenomena in kagome materials.

In this paper, we investigate the electronic structure of the newly discovered kagome superconductor $CsTi_3Bi_5$. By using high resolution laser-based angle-resolved photoemission spectroscopy (ARPES), in combination with the band structure calculations, we have directly observed the characteristic electronic features of the kagome lattice. We directly observed the flat band derived from the destructive interferences of the Bloch wave func-

tions within the kagome lattices. We also identify the Dirac nodal loops and nodal lines in three dimensional momentum space. The Z2 nontrivial topological surface states are also observed. Such coexistence of multiple nontrivial band structures in one kagome superconductor provides a new platform to study the rich physics in the kagome lattice.

CsTi₃Bi₅ single crystals were grown using a self flux method[28]. Typical CsTi₃Bi₅ crystals with a lateral size of ~ 3 mm and regular hexagonal morphology were obtained. High resolution angle-resolved photoemission measurements were performed using a lab-based ARPES system equipped with the 6.994 eV vacuum-ultra-violet (VUV) laser and a hemispherical electron energy analyzer DA30L (Scienta-Omicron)[29, 30]. The laser spot is focused to around 10 μ m on the sample in order to minimize the influence of sample inhomogeneity. The light polarization can be varied to get linear polarization along different directions. In the LV (LH) polarization the electric vector of the laser light is perpendicular (parallel) to the plane formed by the light path and the analyzer lens axis. The energy resolution was set at 1 meV and the angular resolution was 0.3 degree corresponding to 0.004 \AA^{-1} momentum resolution at the photon energy of 6.994 eV. All the samples were cleaved *in situ* at a low temperature of 20 K and measured in ultrahigh vacuum with a base pressure better than 5×10^{-11} mbar. The Fermi level is referenced by measuring on clean polycrystalline gold that is electrically connected to the sample.

Density functional theory (DFT) calculations with projector augmented-wave pseudopotential method[31] are implemented through Vienna ab initio simulation package (VASP)[32]. The exchange correlation functional is treated by Perdew-Burke-Ernzerh (PBE) of parameterization of generalized gradient approximation (GGA)[33]. The convergence criterion of atomic forces in structural optimization with VASP is less than 1 meV/\AA total energy convergence threshold of all processes is 10^{-6} eV/atom. The cutoff energy of the plane-wave is set as 520 eV. The Γ centered $20 \times 20 \times 12$ Monkhorst-Pack k-point grid is used in the self-consistent cycle. Wannier90 package[34] is used to fit Wannier functions and construct tight-binding models, and WannierTools[35] package is used to calculate the surface spectral functions by using the surface Green's function method. Calculations of structures' parity are performed through a combination of the irvsp program[36] and VASP.

Figure 1d shows the Fermi surface mapping of CsTi₃Bi₅ measured at 20 K. The entire first BZ is covered by our laser ARPES measurements. Five Fermi surface sheets are clearly observed, as quantitatively shown in Fig. 1e. The Fermi surface consists of three electron-

like Fermi surface sheets around $\bar{\Gamma}$ (α , β and γ_1 in Fig. 1e), an electron-like triangular Fermi pocket around \bar{K} (γ_2 in Fig. 1e) and a small hole-like Fermi pocket around \bar{M} (δ in Fig. 1e).

In order to understand the measured electronic structure, we carried out detailed band structure calculations. Figs. 1f and 1g show the calculated band structures of CsTi₃Bi₅ without considering the spin orbit coupling (SOC) (Fig. 1f) and considering SOC (Fig. 1g). These calculations project the band structures onto different Ti 3d orbitals along high symmetry directions in the BZ. The low energy bands are mainly from the 3d orbitals of titanium. The characteristic electronic features of a kagome lattice, including the flat band, two saddle points at \bar{M} and a Dirac point at \bar{K} , can be clearly observed as marked in Figs. 1f and 1g. These features are mainly from the Ti 3d_{*x*²-*y*²/*xy*} orbitals (red lines in Figs. 1f and 1g) except that the saddle point VHS1 is from Ti 3d_{*z*²} (green line in Figs. 1f and 1g). The consideration of SOC shows little effect on the flat band and the saddle points but opens a gap at the Dirac points (Fig. 1g).

The calculated band structures of CsTi₃Bi₅ (Figs. 1f and 1g) are very similar to that of CsV₃Sb₅ where the kagome lattice related electronic features are mainly from the V 3d orbitals[13, 37]. The main difference is the band position with respect to the Fermi level. In CsTi₃Bi₅ the kagome lattice related bands are shifted upwards by ~ 1 eV when compared with those in CsV₃Sb₅. This is because CsTi₃Bi₅ has one electron less per Ti per unit cell than that of CsV₃Sb₅ when Ti is replaced by V. As a result, although the Ti 3d orbitals still dominate the density of states (DOS) around the Fermi level E_F , the two van Hove singularities (VHS) in CsTi₃Bi₅ are above the Fermi level whereas they are close or below the Fermi level in CsV₃Sb₅[38, 39]. This provides a possible explanation of the absence of the CDW order in CsTi₃Bi₅. The upward band shift also moves the flat band close to Fermi level in CsTi₃Bi₅.

Figure 1h shows the calculated Fermi surface in the three dimensional Brillouin zone. The Fermi surface consists of five sheets which are quite two dimensional. This is expected due to the strong in-plane bonding and weak interlayer coupling in CsTi₃Bi₅ which is similar to that in CsV₃Sb₅. The calculated Fermi surface at $k_z=0$ is shown in Fig. 1i. To make a better comparison between the measured Fermi surface and band structures with the band structure calculations, we find that the Fermi level of the calculated band structures needs to be shifted downwards by ~ 90 meV, as shown in Figs. 1f and 1g. The calculated Fermi

surface (Figs. 1h and 1i) shows an excellent agreement with the measured results in Figs. 1d and 1e.

Nontrivial Flat Band

For the genuine kagome lattice, it shows a perfect flat band across the entire Brillouin zone, as schematically shown in Fig. 2g. In real kagome materials like CsTi_3Bi_5 , as shown in Figs. 1f and 1g, the flat band (FB) is nearly dispersionless along $\bar{K}-\bar{M}-\bar{K}$ but becomes dispersive along $\bar{\Gamma}-\bar{M}$ and $\bar{\Gamma}-\bar{K}$ directions. This is because, in real kagome materials, the flat band dispersion can be modified by additional factors besides the spin orbit coupling, such as the in-plane next-nearest-neighbor hopping, the interlayer coupling or the multiple orbital degrees of freedom. So far there have been some ARPES studies reporting the observation of the kagome lattice-derived flat band in GdV_6Sn_6 [40], YMn_6Sn_6 [41], CoSn [42–44], Fe_3Sn_2 [45] and FeSn [46]. However, there is little clear evidence reported about the kagome-derived flat band in the 135 family represented by AV_3Sb_5 ($\text{A}=\text{K}, \text{Rb}$ or Cs).

Figure 2a and 2b show the band structures of CsTi_3Bi_5 measured at 20 K along the $\bar{\Gamma}-\bar{M}-\bar{K}-\bar{\Gamma}$ high symmetry directions under the LV (Fig. 2a) and LH (Fig. 2b) light polarizations. In order to resolve all the band structures more clearly, the corresponding second derivative image is shown in Fig. 2c. There seems to be a dispersionless band across the entire Brillouin zone at the binding energy of ~ 220 meV. A careful analysis indicated that this band consists of two different parts. The first part is marked by the red dashed line in Fig. 2c while the rest of the band represent the second part. As compared with the band structure calculations in Figs. 2d and 2e, the first part shows a good agreement with the flat band from the band structure calculations. This indicates that it is kagome lattice derived flat band. This band can be attributed to the local destructive interferences of the Bloch wave functions within the kagome lattices (Fig. 2f). The second part of the dispersionless band at ~ 220 meV is not expected from the band structure calculations (Figs. 2d and 2e). A careful inspection indicates that there is an additional spectral weight buildup in the binding energy range of $220\sim 500$ meV. The two energies happen to coincide with the top and bottom energy positions of the first part flat band. This indicates that the extra spectral weight buildup is closely related to the first part flat band. The second part flat band at ~ 220 meV actually represents a spectral weight cut-off at this energy (see Fig. S1 in Supplementary Materials for details).

Dirac Nodal Lines

In some quantum materials, the bands can cross at a discrete point in the momentum space, forming Dirac point with spin degeneracy or Weyl point with spin polarization. The Dirac points can also form nodal lines and nodal loops in three dimensional momentum space[47]. The Dirac points can be categorized into three types according to the slopes of the involved bands[48, 49]. The materials, which have the electronic structure with the type-II (two dispersion branches exhibit the same sign of slope) or type-III (one of two branches is dispersionless) Dirac points, may host exotic properties, e.g., the chiral anomaly[48] and Klein tunneling[50]. However, there have been few established cases of the type-II and type-III Dirac point realization in real materials, not to mention their simultaneous observation in one material.

Figure 3a and 3b show our identification of two sets of Dirac nodal loops and one set of Dirac lines in CsTi_3Bi_5 . Fig. 3a shows the calculated band structure along the high-symmetry directions without considering spin-orbit coupling. We can find two groups of linear dispersion crossings in a covered energy region around E_F , marked as NL1 and NL2 in Fig. 3a. Our DFT calculations reveal that these Dirac nodes are not isolated, but form multiple nodal loops in $k_z=0$ and $k_z=\pi/c$ planes as seen in Fig 3b. The NL1 type-II nodal loops form in-plane hexagons centered on Γ and A while the NL2 nodal loops form in-plane triangles centered on all the K and H points. These nodal loops are protected by the M_z mirror symmetry. Detailed band analysis shows that the type-II NL1 of $k_z=0$ and $k_z=\pi/c$ planes are not connected along the k_z direction due to the absence of mirror symmetry between $0 < k_z < \pi/c$. However, for the type-III NL2 in the $k_z=0$ and $k_z=\pi/c$ planes, we find another set of nodal lines in the Γ -K-H-A plane that links them. These nodal lines are type-III and protected by the M_x mirror symmetry. Due to the six-fold rotational symmetry, there are six nodal lines and NL2 loops that are symmetrically distributed near K and L points. Slices at different k_z positions have similar band structures, which makes these nodal loops in different slices still possible to be captured experimentally in spite of the opening of small gaps. Moreover, after considering SOC, these nodal loops will further open gaps but the gap size remains small ($< 50\text{meV}$).

Figure 3c to 3e show the measured band structures along $\bar{\Gamma}-\bar{M}$, $\bar{M}-\bar{K}$ and $\bar{K}-\bar{\Gamma}$ high-symmetry directions, respectively. For comparison, the corresponding calculated band structures with SOC are presented in Figs. 3f to 3h. The calculated bands agree very well with the experimental results. The NL1 point is formed by the crossing of the β and γ_1 bands,

as shown by the blue and red dashed lines in Figs. 3c and 3e. These two bands (β and γ_1) share the same sign of slope along both $\bar{\Gamma}$ - \bar{M} (Fig. 3c) and $\bar{\Gamma}$ - \bar{K} (Fig. 3e) directions, forming a type-II Dirac nodal loop. The NL2 point is formed by the crossing of the γ_2 band and the kagome flat band, as shown by the blue and red dashed lines in Figs. 3d and 3e. Since the kagome flat band is nearly dispersionless, the NL2 Dirac nodal loop can be categorized into type-III.

Nontrivial Topological Surface States

The spin-orbit coupling is stronger in CsTi_3Bi_5 than that in CsV_3Sb_5 because of the heavy element Bi. We also note that the calculated energy bands give rise to a strong topological Z2 index since the PT symmetry is conserved in CsTi_3Bi_5 (see Fig. S3 in Supplementary Materials)[27, 28]. This will result in possible topologically nontrivial surface states. Fig. 4a shows the band structure measured around $\bar{\Gamma}$ along the \bar{M} - $\bar{\Gamma}$ - \bar{M} direction under the LV light polarization. The corresponding second derivative image is shown in Fig. 4b. For comparison, Figs. 4c and 4d show the calculated band structures without and with SOC, respectively, along the same momentum cut. All the observed bands in Fig. 4b can be well assigned by comparing with the calculated bands (as shown by coloured lines in Figs. 4b and 4d) except for one band that is marked as TSS in Fig. 4b. In order to understand its origin, we analyzed the energy bands in details. We find that CsTi_3Bi_5 has symmetry-protected band degeneracy along the Γ -A path between the γ and β bands, as well as between the β and α bands, giving rise to multiple topological Dirac semimetal states (see Fig. S3 in Supplementary Materials). This type of topological Dirac semimetal states also appear in AV_3Sb_5 near the Fermi level along the Γ -A path. However, in CsTi_3Bi_5 , continuous band gaps throughout the whole Brillouin zone exist between the ϵ and δ bands, as well as between the δ and γ bands. Combining the time-reversal and inversion symmetries in CsTi_3Bi_5 , we obtain nontrivial Z2 topological invariant of ϵ and δ bands by calculating the parity of the wavefunctions at all time-reversal invariant momenta (TRIM)[51], as seen in Fig. S3 in Supplementary Materials. Moreover, band gaps and band inversions due to the strong SOC of the system can induce additional Dirac topological surface states (TSS) crossing at the TRIM Γ point as seen in the surface spectral function of Figs. 4e and 4f. Comparing with the bands in Fig. 4d, we can identify that the topological surface states are located between the ϵ and δ bands, which indicates that they are topologically protected by the nontrivial Z2 invariant. This TSS band gives a good match with the unassigned band in Fig. 4b.

Therefore, we provide a definitive spectroscopic evidence that nontrivial topological surface states exist in the kagome superconductor CsTi_3Bi_5 .

In summary, by using high resolution laser based ARPES in combination with the DFT band structure calculations, we investigate the electronic structure of the newly discovered kagome superconductor CsTi_3Bi_5 . The observed Fermi surface and band structures show excellent agreement with the band structure calculations. We have identified multi-sets of nontrivial band structures in CsTi_3Bi_5 including the kagome lattice derived flat band, type-II and type-III Dirac nodal loops and nodal lines, as well as Z2 nontrivial topological surface states. Such coexistence of nontrivial band structures in one kagome superconductor provides a new platform to understand the physics and explore for new phenomena and exotic properties in the kagome materials.

‡These people contribute equally to the present work.

*Corresponding authors: XJZhou@iphy.ac.cn, LZhao@iphy.ac.cn, hjgao@iphy.ac.cn, gsu@ucas.ac.cn

-
- [1] Subir Sachdev. Kagome and triangular-lattice Heisenberg antiferromagnets: Ordering from quantum fluctuations and quantum-disordered ground states with unconfined bosonic spinons. *Physical Review B*, 45(21):12377–12396, 1992.
 - [2] Patrick A. Lee. An end to the drought of quantum spin liquids. *Science*, 321(5894):1306–1307, 2008.
 - [3] Leon Balents. Spin liquids in frustrated magnets. *Nature*, 464(7286):199–208, 2010.
 - [4] Simeng Yan, David A. Huse, and Steven R. White. Spin-liquid ground state $S=1/2$ of the kagome Heisenberg antiferromagnet. *Science*, 332(6034):1173–1176, 2011.
 - [5] H. M. Guo and M. Franz. Topological insulator on the kagome lattice. *Physical Review B*, 80(11):113102, 2009.
 - [6] Maximilian L. Kiesel and Ronny Thomale. Sublattice interference in the kagome Hubbard model. *Physical Review B*, 86(12):121105, 2012.
 - [7] Maximilian L. Kiesel, Christian Platt, and Ronny Thomale. Unconventional Fermi surface instabilities in the kagome Hubbard model. *Physical Review Letters*, 110(12):126405, 2013.
 - [8] Evelyn Tang, Jia-Wei Mei, and Xiao-Gang Wen. High-temperature fractional quantum Hall

- states. *Physical Review Letters*, 106(23):236802, 2011.
- [9] J. Kubler and C. Felser. Non-collinear antiferromagnets and the anomalous Hall effect. *Europhysics Letters*, 108(6):67001, 2014.
 - [10] Gang Xu, Biao Lian, and Shou-Cheng Zhang. Intrinsic quantum anomalous Hall effect in the kagome lattice $\text{Cs}_2\text{LiMn}_3\text{F}_{12}$. *Physical Review Letters*, 115(18):186802, 2015.
 - [11] Shun-Li Yu and Jian-Xin Li. Chiral superconducting phase and chiral spin-density-wave phase in a Hubbard model on the kagome lattice. *Physical Review B*, 85(14):144402, 2012.
 - [12] Wan-Sheng Wang, Zheng-Zhao Li, Yuan-Yuan Xiang, and Qiang-Hua Wang. Competing electronic orders on kagome lattices at van Hove filling. *Physical Review B*, 87(11):115135, 2013.
 - [13] Brenden R. Ortiz, Samuel M. L Teicher, Yong Hu, Julia L. Zuo, Paul M. Sarte, Emily C. Schueller, A. M Milinda Abeykoon, Matthew J. Krogstad, Stephan Rosenkranz, Raymond Osborn, Ram Seshadri, Leon Balents, Junfeng He, and Stephen D. Wilson. CsV_3Sb_5 : A \mathbb{Z}_2 topological Kagome metal with a superconducting ground state. *Physical Review Letters*, 125(24):247002, 2020.
 - [14] Hui Chen, Haitao Yang, Bin Hu, Zhen Zhao, Jie Yuan, Yuqing Xing, Guojian Qian, Zihao Huang, Geng Li, Yuhan Ye, Sheng Ma, Shunli Ni, Hua Zhang, Qiangwei Yin, Chunsheng Gong, Zhijun Tu, Hechang Lei, Hengxin Tan, Sen Zhou, Chengmin Shen, Xiaoli Dong, Binghai Yan, Ziqiang Wang, and Hong-Jun Gao. Roton pair density wave in a strong-coupling kagome superconductor. *Nature*, 599(7884):222–228, 2021.
 - [15] Yu-Xiao Jiang, Jia-Xin Yin, M. Michael Denner, Nana Shumiya, Brenden R. Ortiz, Gang Xu, Zurab Guguchia, Junyi He, Md Shafayat Hossain, Xiaoxiong Liu, Jacob Ruff, Linus Kautzsch, Songtian S. Zhang, Guoqing Chang, Ilya Belopolski, Qi Zhang, Tyler A. Cochran, Daniel Multer, Maksim Litskevich, Zi-Jia Cheng, Xian P. Yang, Ziqiang Wang, Ronny Thomale, Titus Neupert, Stephen D. Wilson, and M. Zahid Hasan. Unconventional chiral charge order in kagome superconductor KV_3Sb_5 . *Nature Materials*, 20(10):1353–1357, 2021.
 - [16] Xiaokun Teng, Lebing Chen, Feng Ye, Elliott Rosenberg, Zhaoyu Liu, Jia-Xin Yin, Yu-Xiao Jiang, Ji Seop Oh, M. Zahid Hasan, Kelly J. Neubauer, Bin Gao, Yaofeng Xie, Makoto Hashimoto, Donghui Lu, Chris Jozwiak, Aaron Bostwick, Eli Rotenberg, Robert J. Birgeneau, Jiun-Haw Chu, Ming Yi, and Pengcheng Dai. Discovery of charge density wave in a kagome lattice antiferromagnet. *Nature*, 609(7927):490–495, 2022.

- [17] Brenden R. Ortiz, Ldia C. Gomes, Jennifer R. Morey, Michal Winiarski, Mitchell Bordelon, John S. Mangum, Iain W. H. Oswald, Jose A. Rodriguez-Rivera, James R. Neilson, Stephen D. Wilson, Elif Ertekin, Tyrel M. McQueen, and Eric S. Toberer. New kagome prototype materials: discovery of KV_3Sb_5 , RbV_3Sb_5 , and CsV_3Sb_5 . *Physical Review Materials*, 3(9):094407, 2019.
- [18] Shuo-Ying Yang, Yaojia Wang, Brenden R. Ortiz, Defa Liu, Jacob Gayles, Elena Derunova, Rafael Gonzalez-Hernandez, Libor Smejkal, Yulin Chen, Stuart S. P. Parkin, Stephen D. Wilson, Eric S. Toberer, Tyrel McQueen, and Mazhar N. Ali. Giant, unconventional anomalous Hall effect in the metallic frustrated magnet candidate, KV_3Sb_5 . *Science Advances*, 6(31):eabb6003, 2020.
- [19] Qiangwei Yin, Zhijun Tu, Chunsheng Gong, Yang Fu, Shaohua Yan, and Hechang Lei. Superconductivity and normal-state properties of kagome metal RbV_3Sb_5 Single Crystals. *Chinese Physics Letters*, 38(3):037403, 2021.
- [20] Hengxin Tan, Yizhou Liu, Ziqiang Wang, and Binghai Yan. Charge density waves and electronic properties of superconducting kagome metals. *Physical Review Letters*, 127(4):046401, 2021.
- [21] Xilin Feng, Kun Jiang, Ziqiang Wang, and Jiangping Hu. Chiral flux phase in the kagome superconductor AV_3Sb_5 . *Science Bulletin*, 66(14):1384–1388, 2021.
- [22] Jianzhou Zhao, Weikang Wu, Yilin Wang, and Shengyuan A. Yang. Electronic correlations in the normal state of kagome superconductor KV_3Sb_5 . *Physical Review B*, 103(24):L241117, 2021.
- [23] Zuowei Liang, Xingyuan Hou, Fan Zhang, Wanru Ma, Ping Wu, Zongyuan Zhang, Fanghang Yu, J. J. Ying, Kun Jiang, Lei Shan, Zhenyu Wang, and X. H. Chen. Three-Dimensional charge density wave and surface-dependent vortex-core states in a kagome superconductor CsV_3Sb_5 . *Physical Review X*, 11(3):031026, 2021.
- [24] Zhiwei Wang, Yu-Xiao Jiang, Jia-Xin Yin, Yongkai Li, Guan-Yong Wang, Hai-Li Huang, Shen Shao, Jinjin Liu, Peng Zhu, Nana Shumiya, Md Shafayat Hossain, Hongxiong Liu, Youguo Shi, Junxi Duan, Xiang Li, Guoqing Chang, Pengcheng Dai, Zijin Ye, Gang Xu, Yanchao Wang, Hao Zheng, Jinfeng Jia, M. Zahid Hasan, and Yugui Yao. Electronic nature of chiral charge order in the kagome superconductor CsV_3Sb_5 . *Physical Review B*, 104(7):075148, 2021.
- [25] He Zhao, Hong Li, Brenden R. Ortiz, Samuel M. L. Teicher, Takamori Park, Mengxing Ye,

- Ziqiang Wang, Leon Balents, Stephen D. Wilson, and Ilija Zeljkovic. Cascade of correlated electron states in the kagome superconductor CsV_3Sb_5 . *Nature*, 599(7884):216–221, 2021.
- [26] Linpeng Nie, Kuanglv Sun, Wanru Ma, Dianwu Song, Lixuan Zheng, Zuowei Liang, Ping Wu, Fanghang Yu, Jian Li, Min Shan, Dan Zhao, Shunjiao Li, Baolei Kang, Zhimian Wu, Yanbing Zhou, Kai Liu, Ziji Xiang, Jianjun Ying, Zhenyu Wang, Tao Wu, and Xianhui Chen. Charge-density-wave-driven electronic nematicity in a kagome superconductor. *Nature*, 604(7904):59–64, 2022.
- [27] Xin-Wei Yi, Xing-Yu Ma, Zhen Zhang, Zheng-Wei Liao, Jing-Yang You, and Gang Su. Large kagome family candidates with topological superconductivity and charge density waves. *arXiv e-prints*, arXiv:2202.05588, 2022.
- [28] Haitao Yang, Zhen Zhao, Xin-Wei Yi, Jiali Liu, Jing-Yang You, Yuhang Zhang, Hui Guo, Xiao Lin, Chengmin Shen, Hui Chen, Xiaoli Dong, Gang Su, and Hong-Jun Gao. Titanium-based kagome superconductor CsTi_3Bi_5 and topological states. *arXiv e-prints*, arXiv:2209.03840, 2022.
- [29] Guodong Liu, Guiling Wang, Yong Zhu, Hongbo Zhang, Guochun Zhang, Xiaoyang Wang, Yong Zhou, Wentao Zhang, Haiyun Liu, Lin Zhao, Jianqiao Meng, Xiaoli Dong, Chuangtian Chen, Zuyan Xu, and X. J. Zhou. Development of a vacuum ultraviolet laser-based angle-resolved photoemission system with a superhigh energy resolution better than 1 meV. *Review of Scientific Instruments*, 79(2):023105–11, 2008.
- [30] Zhou Xingjiang, He Shaolong, Liu Guodong, Zhao Lin, Yu Li, and Zhang Wentao. New developments in laser-based photoemission spectroscopy and its scientific applications: a key issues review. *Reports on Progress in Physics*, 81(6):062101, 2018.
- [31] P. E. Blochl. Projector augmented-wave method. *Physical Review B*, 50(24):17953–17979, 1994.
- [32] G. Kresse and J. Furthmuller. Efficient iterative schemes for ab initio total-energy calculations using a plane-wave basis set. *Physical Review B*, 54(16):11169–11186, 1996.
- [33] John P. Perdew, Kieron Burke, and Matthias Ernzerhof. Generalized gradient approximation made simple. *Physical Review Letters*, 77(18):3865–3868, 1996.
- [34] Arash A. Mostofi, Jonathan R. Yates, Young-Su Lee, Ivo Souza, David Vanderbilt, and Nicola Marzari. Wannier90: A tool for obtaining maximally-localised Wannier functions. *Computer Physics Communications*, 178(9):685–699, 2008.

- [35] QuanSheng Wu, ShengNan Zhang, Hai-Feng Song, Matthias Troyer, and Alexey A. Soluyanov. WannierTools: An open-source software package for novel topological materials. *Computer Physics Communications*, 224:405–416, 2018.
- [36] Jiacheng Gao, Quansheng Wu, Clas Persson, and Zhijun Wang. Irvsp: To obtain irreducible representations of electronic states in the VASP. *Computer Physics Communications*, 261:107760, 2021.
- [37] Brenden R. Ortiz, Samuel M. L. Teicher, Linus Kautzsch, Paul M. Sarte, Noah Ratcliff, John Harter, Jacob P. C. Ruff, Ram Seshadri, and Stephen D. Wilson. Fermi surface mapping and the nature of charge-density-wave order in the kagome superconductor CsV_3Sb_5 . *Physical Review X*, 11(4):041030, 2021.
- [38] Hailan Luo, Qiang Gao, Hongxiong Liu, Yuhao Gu, Dingsong Wu, Changjiang Yi, Junjie Jia, Shilong Wu, Xiangyu Luo, Yu Xu, Lin Zhao, Qingyan Wang, Hanqing Mao, Guodong Liu, Zhihai Zhu, Youguo Shi, Kun Jiang, Jiangping Hu, Zuyan Xu, and X. J. Zhou. Electronic nature of charge density wave and electron-phonon coupling in kagome superconductor KV_3Sb_5 . *Nature Communications*, 13(1):273, 2022.
- [39] Mingu Kang, Shiang Fang, Jeong-Kyu Kim, Brenden R. Ortiz, Sae Hee Ryu, Jimin Kim, Jonggyu Yoo, Giorgio Sangiovanni, Domenico Di Sante, Byeong-Gyu Park, Chris Jozwiak, Aaron Bostwick, Eli Rotenberg, Efthimios Kaxiras, Stephen D. Wilson, Jae-Hoon Park, and Riccardo Comin. Twofold van Hove singularity and origin of charge order in topological kagome superconductor CsV_3Sb_5 . *Nature Physics*, 18(3):301–308, 2022.
- [40] Shuting Peng, Yulei Han, Ganesh Pokharel, Jianchang Shen, Zeyu Li, Makoto Hashimoto, Donghui Lu, Brenden R. Ortiz, Yang Luo, Houchen Li, Mingyao Guo, Bingqian Wang, Shengtao Cui, Zhe Sun, Zhenhua Qiao, Stephen D. Wilson, and Junfeng He. Realizing kagome band structure in two-dimensional kagome surface states of RV_6Sn_6 ($R = \text{Gd}, \text{Ho}$). *Physical Review Letters*, 127(26):266401, 2021.
- [41] Man Li, Qi Wang, Guangwei Wang, Zhihong Yuan, Wenhua Song, Rui Lou, Zhengtai Liu, Yaobo Huang, Zhonghao Liu, Hechang Lei, Zhiping Yin, and Shancai Wang. Dirac cone, flat band and saddle point in kagome magnet YMn_6Sn_6 . *Nature Communications*, 12(1):3129, 2021.
- [42] Mingu Kang, Shiang Fang, Linda Ye, Hoi Chun Po, Jonathan Denlinger, Chris Jozwiak, Aaron Bostwick, Eli Rotenberg, Efthimios Kaxiras, Joseph G. Checkelsky, and Riccardo Comin.

- Topological flat bands in frustrated kagome lattice CoSn. *Nature Communications*, 11(1):4004, 2020.
- [43] Zhonghao Liu, Man Li, Qi Wang, Guangwei Wang, Chenhaoping Wen, Kun Jiang, Xianglu Lu, Shichao Yan, Yaobo Huang, Dawei Shen, Jia-Xin Yin, Ziqiang Wang, Zhiping Yin, Hechang Lei, and Shancai Wang. Orbital-selective Dirac fermions and extremely flat bands in frustrated kagome-lattice metal CoSn. *Nature Communications*, 11(1):4002, 2020.
- [44] Hao Huang, Lixuan Zheng, Zhiyong Lin, Xu Guo, Sheng Wang, Shuai Zhang, Chi Zhang, Zhe Sun, Zhengfei Wang, Hongming Weng, Lin Li, Tao Wu, Xianhui Chen, and Changgan Zeng. Flat-band-induced anomalous anisotropic charge transport and orbital magnetism in kagome metal CoSn. *Physical Review Letters*, 128(9):096601, 2022.
- [45] Zhiyong Lin, Jin-Ho Choi, Qiang Zhang, Wei Qin, Seho Yi, Pengdong Wang, Lin Li, Yifan Wang, Hui Zhang, Zhe Sun, Laiming Wei, Shengbai Zhang, Tengfei Guo, Qingyou Lu, Jun-Hyung Cho, Changgan Zeng, and Zhenyu Zhang. Flatbands and emergent ferromagnetic ordering in Fe_3Sn_2 kagome lattices. *Physical Review Letters*, 121(9):096401, 2018.
- [46] Mingu Kang, Linda Ye, Shiang Fang, Jhih-Shih You, Abe Levitan, Minyong Han, Jorge I. Facio, Chris Jozwiak, Aaron Bostwick, Eli Rotenberg, Mun K. Chan, Ross D. McDonald, David Graf, Konstantine Kaznatcheev, Elio Vescovo, David C. Bell, Efthimios Kaxiras, Jeroen van den Brink, Manuel Richter, Madhav Prasad Ghimire, Joseph G. Checkelsky, and Riccardo Comin. Dirac fermions and flat bands in the ideal kagome metal FeSn. *Nature Materials*, 19(2):163–169, 2020.
- [47] Chaofan Zhang, Yiwei Li, Ding Pei, Zhongkai Liu, and Yulin Chen. Angle-resolved photoemission spectroscopy study of topological quantum materials. *Annual Review of Materials Research*, 50(1):131–153, 2020.
- [48] Alexey A. Soluyanov, Dominik Gresch, Zhijun Wang, QuanSheng Wu, Matthias Troyer, Xi Dai, and B. Andrei Bernevig. Type-II Weyl semimetals. *Nature*, 527(7579):495–498, 2015.
- [49] Chunyao Song, Lei Jin, Pengbo Song, Hongtao Rong, Wenpei Zhu, Bo Liang, Shengtao Cui, Zhe Sun, Lin Zhao, Youguo Shi, Xiaoming Zhang, Guodong Liu, and X. J. Zhou. Spectroscopic evidence for Dirac nodal surfaces and nodal rings in the superconductor NaAlSi. *Physical Review B*, 105(16):L161104, 2022.
- [50] T. E O'Brien, M. Diez, and C. W. J Beenakker. Magnetic breakdown and Klein tunneling in a type-II Weyl semimetal. *Physical Review Letters*, 116(23):236401, 2016.

- [51] Liang Fu and C. L. Kane. Topological insulators with inversion symmetry. *Physical Review B*, 76(4):045302, 2007.

Acknowledgements

This work is supported by the National Natural Science Foundation of China (Grant No. 11888101, 11922414 and 11974404), the National Key Research and Development Program of China (Grant No. 2021YFA1401800, 2017YFA0302900, 2018YFA0704200, 2018YFA0305600, 2019YFA0308000 and 2022YFA1604200), the Strategic Priority Research Program (B) of the Chinese Academy of Sciences (Grant No. XDB25000000 and XDB33000000), the Youth Innovation Promotion Association of CAS (Grant No. Y2021006) and Synergetic Extreme Condition User Facility (SECUF).

Author Contributions

J.G.Y., Y.Y.X., Z.Z. and X.W.Y. contribute equally to this work. X.J.Z., L.Z., J.G.Y. and Y.Y.X. proposed and designed the research. Z.Z., H.C., H.T.Y., H.T.Y. and H.J.G. contributed to single crystal growth. X.W.Y., J.Y.Y., B.G. and G.S. contribute to the DFT band calculations. T.M.M., H.L.L., H.C., B.L., W.P.Z., S.J.Z, F.F.Z., T.Y., Z.M.W., Q.J.P., H.Q.M., G.D.L., L.Z., Z.Y.X. and X.J.Z. contributed to the development and maintenance of Laser-ARPES system. J.G.Y. and Y.Y.X. carried out the ARPES experiment. J.G.Y., L.Z. and X.J.Z. analyzed the data. J.G.Y., L.Z. and X.J.Z. wrote the paper with H.T.Y., H.J.G. and G.S.. All authors participated in the discussion and comment on the paper.

Additional information

Competing financial interests: The authors declare no competing financial interests.

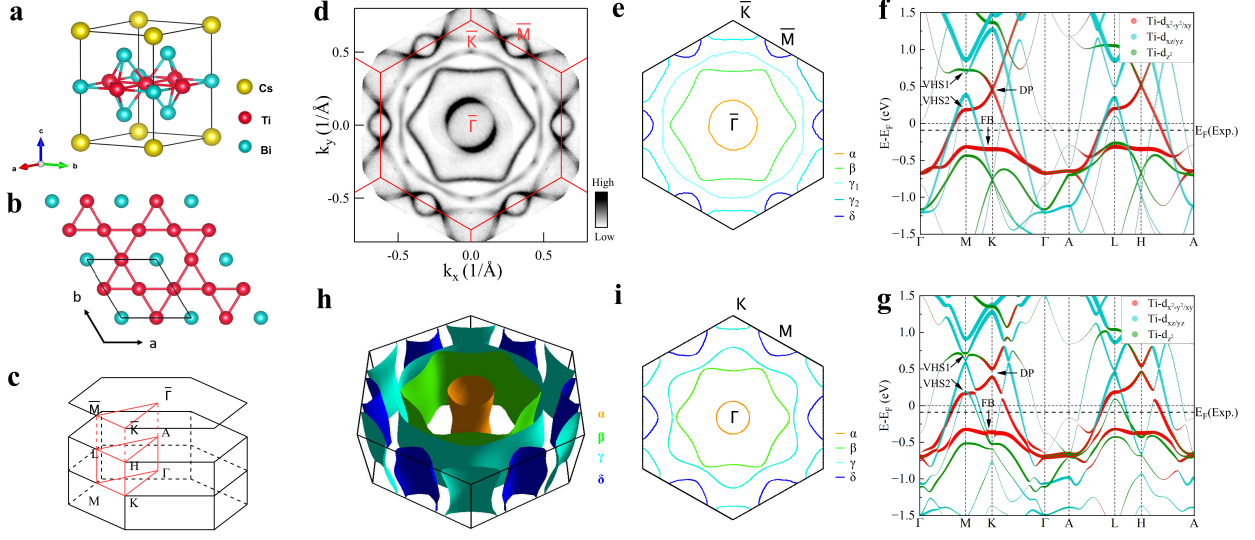


FIG. 1: **Fermi surface and calculated band structures of CsTi_3Bi_5 .** **a** Schematic pristine crystal structure of CsTi_3Bi_5 . **b** Top view of the crystal structure with a two-dimensional kagome lattice of Titanium. **c** Three-dimensional Brillouin zone with high-symmetry points and high-symmetry momentum lines marked. **d** Fermi surface mapping of CsTi_3Bi_5 measured at a temperature of 20 K. It is obtained by integrating the spectral intensity within 10 meV with respect to the Fermi level and symmetrized assuming six-fold symmetry. Five Fermi surface sheets are clearly observed and quantitatively shown in **e**. Three Fermi surface sheets are around the Brillouin zone center Γ marked as α (orange line), β (green line) and γ_1 (light blue line). One Fermi surface is around the K point marked as γ_2 (blue line) and one is around the M point marked as δ (dark blue line). **f** Calculated band structure along high-symmetry directions without considering SOC. Different colors represent different orbital components of Ti_{3d} . **g** Same as **f** but considering SOC. The flat band (FB), two saddle points (VHS1 and VHS2) and a Dirac point (DP) are marked by arrows. To make a better comparison with measured results, the Fermi level is shifted downwards by 90 meV, as shown by the dashed lines in **f** and **g**. **h** Calculated three dimensional Fermi surface based on the first principle DFT calculations. The Fermi surface sheets are quite two dimensional. The calculated Fermi surface at $k_z=0$ is shown in **i**. The measured Fermi surface (**d**) shows an excellent agreement with the calculated one (**i**).

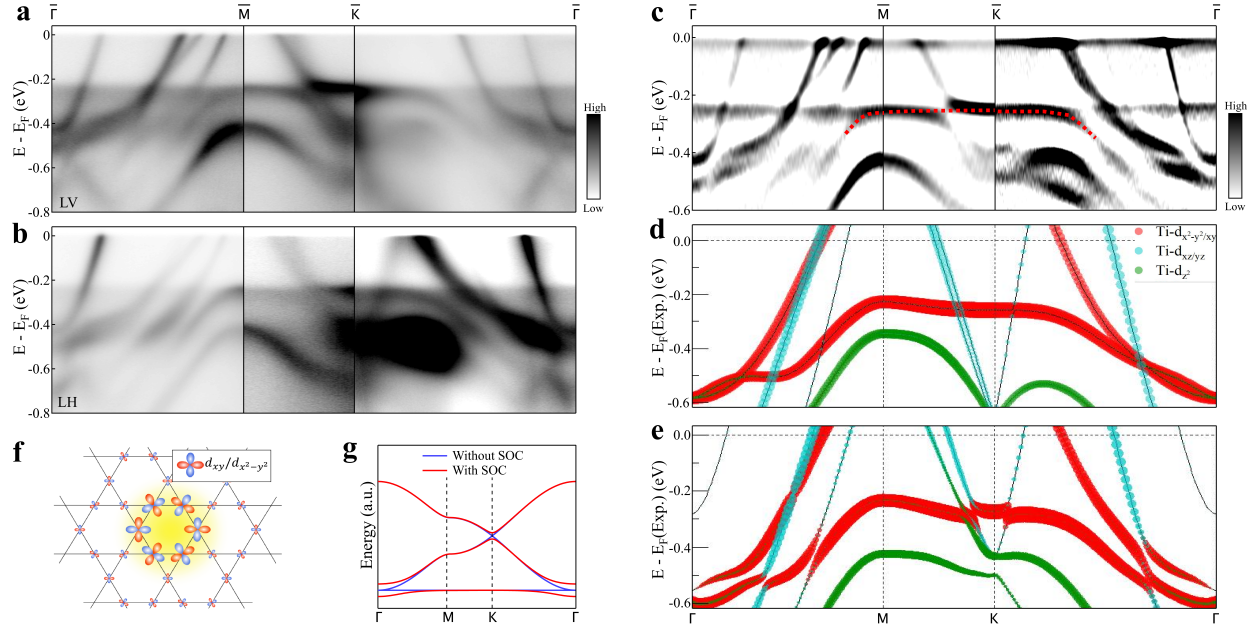


FIG. 2: **Direct observation of flat band in CsTi_3Bi_5 .** **a,b** Detailed band structures measured along the $\bar{\Gamma}$ - \bar{M} - \bar{K} - $\bar{\Gamma}$ high symmetry directions under two different polarization geometries, LV (**a**) and LH (**b**). **c** Second derivative image with respect to energy obtained from **a,b** in order to resolve the band structures more clearly. The red dashed line highlights the observed flat band. **d** The corresponding calculated band structure along the Γ -M-K- Γ high-symmetry directions without considering SOC. Different colors represent different orbital components of Ti_{3d} . **e** Same as **d** but considering SOC. **f** Orbital textures of the effective Wannier states giving rise to the flat bands with $d_{xy}/d_{x^2-y^2}$ orbitals. **g** Tight-binding band structures of kagome lattice with (red lines) and without (blue lines) SOC. Inclusion of the spin orbit coupling gaps both the Dirac crossing at K and the quadratic touching between the flat band and the Dirac band around Γ .

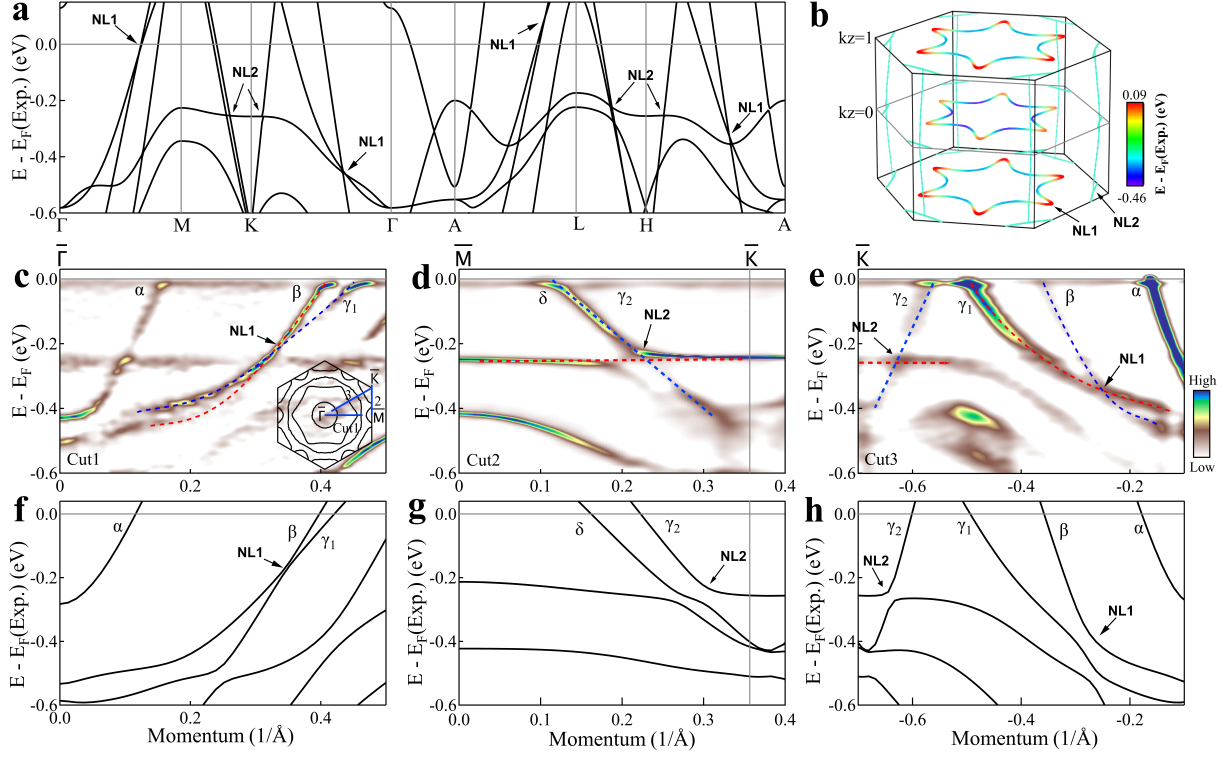


FIG. 3: **Calculated and observed Dirac nodal points in CsTi_3Bi_5 .** **a** Calculated band structures along high-symmetry directions without considering SOC. Two sets of Dirac nodal points (NL1 and NL2) are identified as marked by arrows. **b** Formation of the Dirac nodal lines in three dimensional momentum space. The NL1 Dirac points form hexagonal Dirac nodal loops around Γ in the $k_z=0$ plane and A in the $k_z=1$ plane. The NL2 Dirac points form triangular Dirac nodal loops around K in the $k_z=0$ plane and H in the $k_z=1$ plane as well as six nodal lines along the k_z direction. The detailed distribution of the NL1 and NL2 Dirac nodal lines in three-dimensional momentum space is shown in Fig. S2 in Supplementary Materials. **c-e** Band structures measured along $\bar{\Gamma}-\bar{M}$ (Cut1), $\bar{M}-\bar{K}$ (Cut2) and $\bar{K}-\bar{\Gamma}$ (Cut3), respectively. The location of the momentum cuts is shown in the inset of **c** by the blue lines. These images are obtained by taking second derivative curvature of the original data. The blue and red dashed lines are guide lines of the two crossing bands. **f-h** The corresponding calculated band structures with SOC. The presence of the Dirac points is marked by arrows.

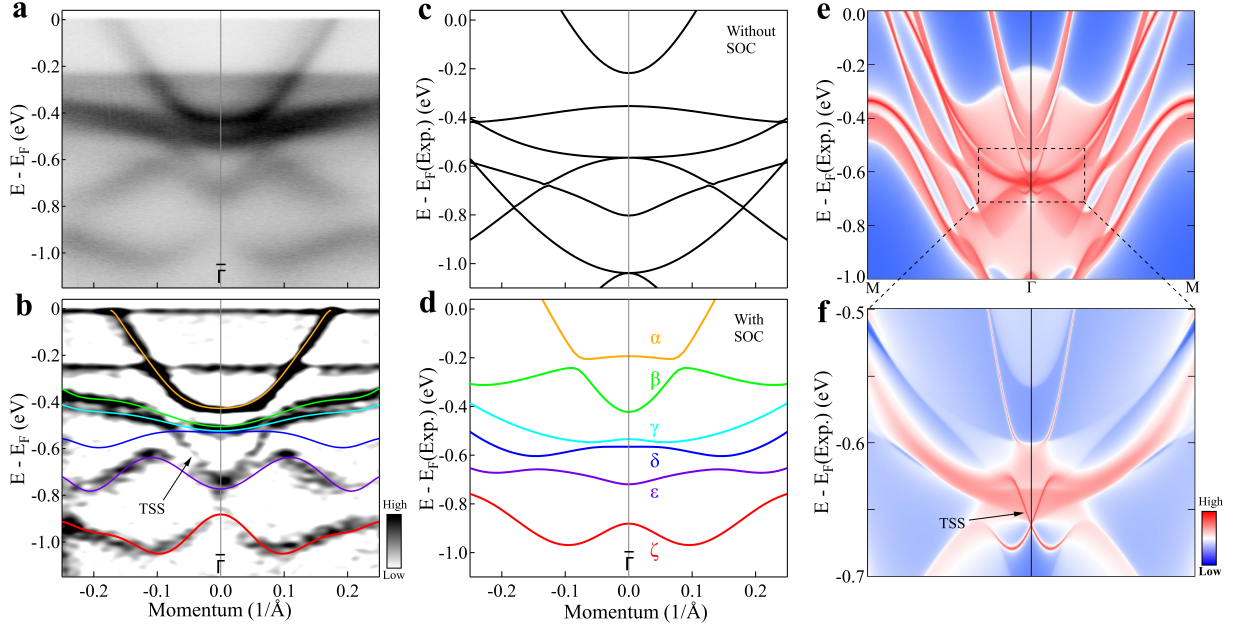


FIG. 4: **Observation of topological surface states in CsTi_3Bi_5 .** **a** Band structure measured around $\bar{\Gamma}$ along the \bar{M} - $\bar{\Gamma}$ - \bar{M} direction under LV polarization geometry. **b** Second derivative image of **a**. The observed six bands are highlighted by different colored lines. The observed topological surface state (TSS) is marked by an arrow. **c-d** The corresponding calculated band structures without (**c**) and with (**d**) SOC. The topological surface state emerges between the δ and ϵ bands which arise from band inversion due to SOC. **e** Calculated surface spectral function along \bar{M} - $\bar{\Gamma}$ - \bar{M} paths projected on the (001) plane for the Bi-terminated CsTi_3Bi_5 . **f** Enlarged view of the topological surface states (TSS) in **e**.